

NIR/Optical Counterparts of Hotspots in Radio Galaxies

K.-H. Mack^{1,?}, M.A. Prieto², G. Brunetti¹, M. Orienti^{2,1}

¹INAF-Istituto di Radioastronomia, Via P. Gobetti 101, I-40129 Bologna, Italy

²Instituto de Astrofísica de Canarias, c/ Vía Láctea s/n, E-38205 La Laguna (Tenerife), Spain

Accepted Received ...; in original form

ABSTRACT

We present new high spatial resolution VLT and VLA observations of a sample of nine low-power ($P_{1.4\text{GHz}} \sim 10^{25}$ W/Hz) radio hotspots. Infrared/optical emission is definitely detected in four of the nine observed objects, resulting in a detection rate of at least 45%. This emission is interpreted as synchrotron radiation from the electrons accelerated in the hot spots. The integrated spectra of these hotspots reveal typical break frequencies between 10^5 and 10^6 GHz, two orders of magnitude higher than typically found in high-power hotspots. This supports the idea that in low-power hotspots with their relatively low magnetic field strengths electrons emit most of their energy at higher frequencies. A simple spectral ageing analysis would imply that the emitting electrons have been injected into the hotspot volume less than 10^3 years ago. We discuss possible scenarios to explain the lack of older electrons in the hotspot region. In particular, the extended morphology of the NIR/optical emission would suggest that efficient re-acceleration mechanisms rejuvenate the electron populations.

Key words: galaxies: active - jets, radio continuum: galaxies

1 INTRODUCTION

Radio hotspots are regions of enhanced radio emission located at the end of the radio lobes of powerful radio sources. These remote bright regions (usually at several hundred kpc away from the galaxy core) mark the “working surface” of supersonic jets in which their kinetic energy is dissipated into the acceleration of relativistic particles. These relativistic particles are left behind forming the extended diffuse radio lobes while the hotspots advance into the ambient medium. As such, hotspots represent the end point of an energetic jet: how the energy of the central radio source is transported, released and maintained in such remote regions are still open questions. However, being relatively isolated regions – away from the central galaxy core – hotspots are ideal laboratories for testing the energetics and the evolution of a radio galaxy.

The synchrotron spectral energy distribution between the radio and optical regime within hotspots, and their radio morphology and polarisation suggest that the relativistic electrons are accelerated at the shocks that form due to the impact of the relativistic jets into the ambient medium (e.g. Meisenheimer 2003). In the context of this scenario the resulting synchrotron spectrum is expected to steepen at higher frequencies due to the severe radiative losses that electrons experience downstream of the shock region (Heavens & Meisenheimer 1987). This is also the reason why optical detections of hotspots are still relatively rare although more observations have been performed since the first detections at visual wavelengths (e.g., Meisenheimer & Röser 1996; Meisenheimer, Yates & Röser

1997; Lähteenmäki & Valtaoja 1999; Brunetti et al. 2001; Prieto, Brunetti & Mack 2002; Cheung, Kim & Song 2005).

At higher frequencies, in the X-ray regime, the search for counterparts of radio hotspots turned out to be more successful. Since the initial X-ray detection of the Cygnus A hotspots by Harris, Carilli & Perley (1994), many hotspots were found to emit X-rays (e.g., Hardcastle 2003). Many of these detections could be explained with synchrotron self-Compton (SSC) emission with the magnetic field strength close to the equipartition value. A significant number of X-ray emitting hotspots however appears to have a larger X-ray intensity than predicted by SSC. This excess could be explained by a magnetic field strength much lower than equipartition, IC emission from the decelerating jet (Georganopoulos & Kazanas 2003) or an additional synchrotron component (Hardcastle et al. 2004). In particular, it has been shown by the latter authors that the more luminous hotspots tend to show SSC emission, while the weaker radio hotspots emit the extra synchrotron component. Both X-ray and optical synchrotron emission from hotspots offer the opportunity to study several of their characteristics which have a number of fundamental implications for the acceleration of relativistic particles in general. They imply either a loss-free transport to the hotspot (e.g. Kundt 1996), or an in-situ production of energetic particles with Lorentz factors $> 10^5$ (e.g. Meisenheimer et al. 1989). Transport from the nucleus is however limited by the unavoidable inverse Compton losses experienced by the electrons in the relativistic jet (Gopal-Krishna et al. 2001). This makes it difficult to explain the optical emission from hot spots at sufficiently large distance (i.e. $> 150 - 200$ kpc) from the nucleus (Brunetti et al. 2003) with this scenario.

In a seminal paper Meisenheimer et al. (1997) discussed the

? E-mail: mack@ira.inaf.it

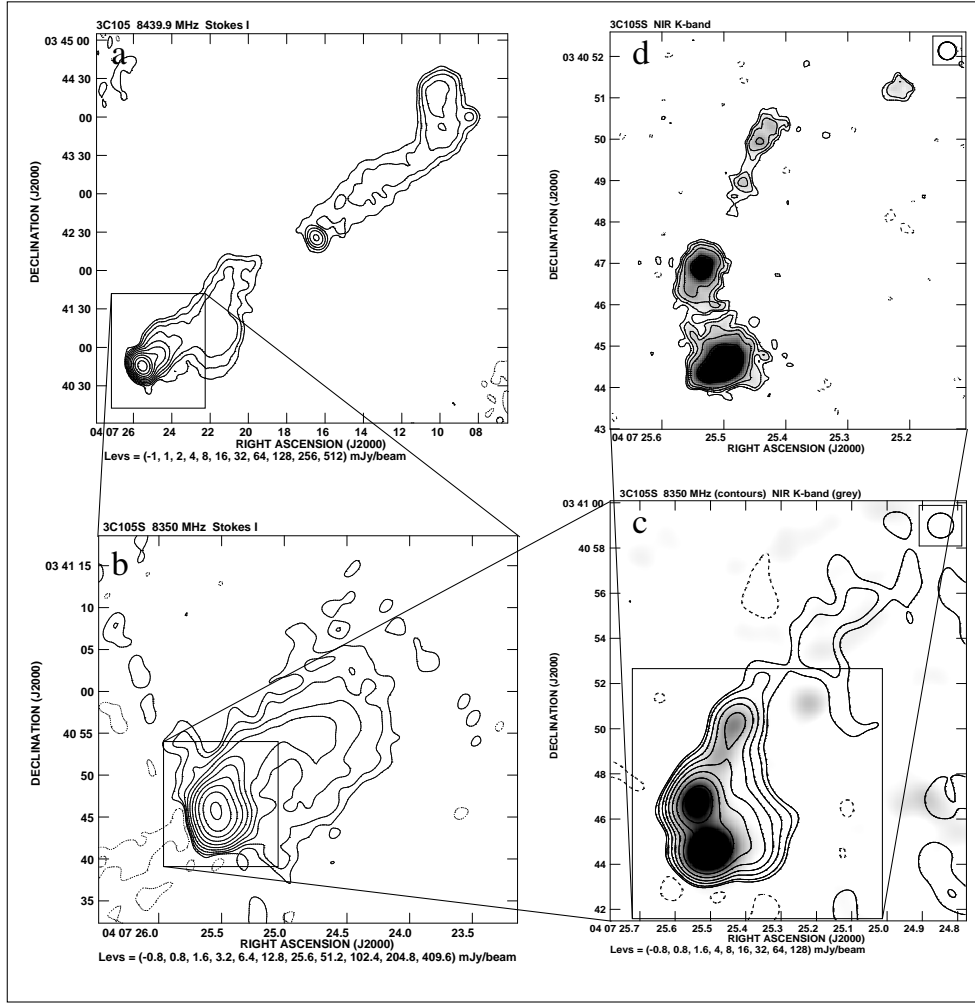


Figure 1. a) 3C 105: entire source, 8.3 GHz, VLA D-array; b) 3C 105S: 8.3 GHz, VLA BC-array; c) 3C 105S: superposition of VLA A-array data (contours) and ISAAC K-band image (grey), both smoothed to a common resolution of $1''.1 \times 1''.1$; d) 3C 105S: NIR K-band emission in original resolution ($0''.43$).

synchrotron spectra of hotspots, from radio to optical, through the analysis of a sample of eight hotspots. Most of these hotspots have spectra that could in principle be accommodated within the standard diffusive shock acceleration model (Bell 1978) on the basis of the observed radio photon spectral index of -0.5 ($S_\nu \propto \nu^{-0.5}$). In the context of this scenario two other characteristics which describe the spectral shape once the electrons have been accelerated are the break frequency, i.e. the maximum energy of the oldest electron population in the hotspot volume, driven by the cooling of the electrons in the post-shock region, and the cut-off frequency, generated by the competition between acceleration and loss mechanisms in the shock region. Observationally, the radiation spectral indices typically increase by $\Delta\alpha \approx 0.5$ beyond the break frequency, and an exponential spectral cut-off develops at the cut-off frequency. Brunetti et al. (2003) have shown that the magnetic field strengths are the weaker, the higher the break and the cut-off frequencies are, with a scaling between break frequency and hotspot magnetic field in the form $\nu_b \propto B^{-3}$ in agreement with theoretical expectations based on the shock-acceleration model. Remarkably, the consequence is that the weaker the magnetic field strengths are, the greater the probability is to find hotspots with counterparts at optical wavelengths (Blundell et al. 1999).

There are however cases of hotspots that do not fit in the

shock-acceleration scenario, at least in its simplest form. The extraordinary spectra of some hot spots, lacking any indication of synchrotron ageing (e.g., 3C390.3, Prieto & Kotilainen 1997; 3C303, Meisenheimer et al. 1997), and/or showing optical extension (e.g., Pictor A, Thomson, Crane & Mackay 1995; 3C445, Prieto et al. 2002), call for an efficient re-acceleration mechanism in situ: basically, the *continuous* work of smoothly distributed accelerators at different points along the hotspot region.

This paper is the third in a series of articles reporting the results of a project aimed at putting studies of spectral emission from hotspots on a broader statistical fundament. In our first paper (Prieto et al. 2002) we showed the optical images made of the southern hotspot of 3C 445. These images revealed bright knots embedded in diffuse optical emission distributed along the region of the impact of the jet into the intergalactic medium, and suggested that continuous re-acceleration of electrons (Fermi-II) is at work in this hotspot in addition to the prime (Fermi-I) acceleration mechanism. The second paper (Brunetti et al. 2003) focused on the statistical aspects of optically detected hotspots identifying the magnetic field strength in hotspots as the key parameter which determines the probability of their detection at optical wavelengths. The present paper compiles the complete set of optical data from VLT ISAAC and FORS observations, complemented by high-resolution radio images on a

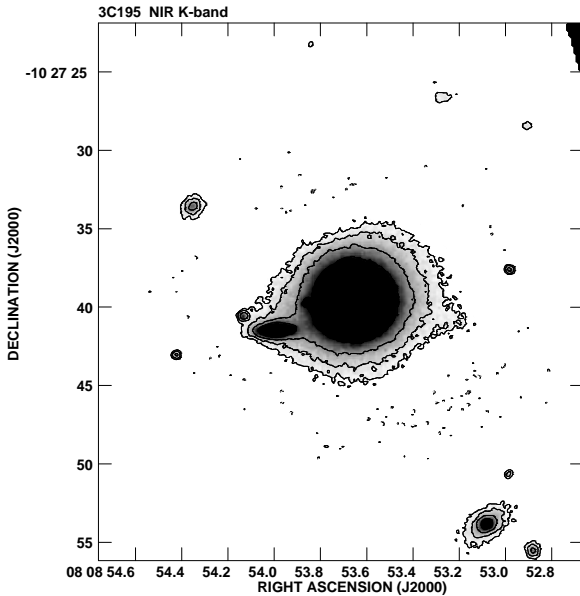


Figure 2. 3C195, the host galaxy in K-band. The elongated structure in east-west direction discussed by Neff et al. (1995) is a superimposed spiral galaxy in combination with a stellar-like object.

sample of candidate objects. In Sect. 2 we describe the selection of our sample and introduce the target sources, Sect. 3 gives the details of the observations and the data analysis. In Sect. 4 we show the results for the individual targets. In Sect. 5 we compare the optical magnitudes with the corresponding radio data. A summary is presented in Sect. 6. Throughout the paper we use the following cosmological parameters: $H_0 = 71 \text{ km s}^{-1} \text{ Mpc}^{-1}$, $\Omega_\Lambda = 0.73$, $\Omega_M = 0.27$.

2 SELECTION OF THE SAMPLE

We constructed a sample of hotspots that could be sufficiently bright to be detected at the VLT. The source list is selected from the complete sample of radio galaxies presented by Tadhunter et al. (1993) which contains 54 sources with measured redshifts $z < 0.7$ and $25 < \delta < 10$ taken from the Wall & Peacock (1985) 2.7-GHz sample. All these sources have been visually inspected using high-resolution maps published by Morganti, Killeen & Tadhunter (1993), Morganti et al. (1999), Kapahi et al. (1998), Leahy et al. (1997) and Hardcastle et al. (1998). In view of the expected anticorrelation of detection probability and magnetic field strength (Blundell et al. 1999; Brunetti et al. 2003) we have a priori excluded the brightest and most compact radio hotspots which emit most of their energy at low frequencies (radio/mm-band). Then we adopted a basic synchrotron model for each radio hotspot by assuming a power law spectrum with injection spectral index $\alpha = 0.6$ and a radiative break, with $\Delta\alpha = 0.5$, at a frequency between the radio and the NIR/optical band (e.g. Meisenheimer et al. 1997). We finally used the normalization of the synchrotron spectrum given by the radio data for each hotspot and assumed a cut-off frequency of their synchrotron spectrum at $\nu = 3 \cdot 10^4 \text{ Hz}$. A final sample of 10 radio hotspots turned out to be sufficiently bright to favour a significant detection in the NIR with VLT. The selected objects are

up to 3 orders of magnitude less luminous (Tab. 4) than the bright and compact hotspots in Cygnus A ($P_{8.3\text{GHz}} = 10^{26} \text{ W=Hz}$).

For all of them, high resolution (up to $0.2''$ FWHM) radio maps were obtained by us or collected from the literature and are used for comparison. In the following we also present maps at lower resolution to show the large-scale morphological context of the more detailed high-resolution maps of the hotspots. We also refer the reader to the images presented by Black et al. (1992) [for 3C 227 and 3C 403], Leahy et al. (1997) [for 3C 105, 3C 327, 3C 445] and Neff, Roberts & Hutchings (1995) [for 3C 195] for further information on the overall structure of the sources.

2.1 The target sample - Radio properties

2.1.1 3C 105

3C 105 at redshift $z = 0.089$ is hosted by a Narrow Line Radio Galaxy (Tadhunter et al. 1993). The most striking properties of this source are the protusions in northern and southern direction of the northern and southern lobes, respectively. These could be interpreted as remainders of a previous jet direction. Both hotspots are well-defined with the southern one much brighter than its northern counterpart (see also Fig. 7 in Leahy et al. 1997). For our near-infrared detection experiment we have selected the southern hotspot complex (Fig. 1). Leahy et al. (1997) interpret the two northern components of this complex morphology as jet emission. In their scenario, the true jet termination hotspot would be the knot at $\alpha = 04^h 07^m 25^s.6$ and $\delta = 03^\circ 40' 46''$, while the southernmost knot is supposed to be formed by a recent disconnection event (Cox et al. 1991), i.e. through the impact of a spinning jet on ambient material of the cocoon wall, subsequent deceleration and formation of a new shock front. The rich substructure of this hotspot is seen as an indication of a rapidly evolving, transient system, presumably influenced by the superposition of a collimated backflow structure (Leahy et al. 1997).

2.1.2 3C 195

With a redshift of $z = 0.11$ the Narrow-Line Radio Galaxy (Morganti et al. 1997) 3C 195 is the most distant source in our sample. Neff et al. (1995) describe it as a large double-lobe source with bright hotspots and a complex lobe structure, suggesting small changes of the radio axis. The optical protrusion, or jet, orthogonal to the radio axis, noted by these authors, turns out to be an underlying spiral galaxy as can be seen at higher resolution (Fig. 2). Both, southern and northern hotspot, were selected as targets for the VLT observations (Fig. 3).

2.1.3 3C 227

3C 227 is a Broad-Line Galaxy (Simpson et al. 1996) at redshift $z = 0.0861$. Black et al. (1992) noted that there is no obvious jet detection in either lobe. The hotspots in both lobes have a complex morphology. The western one consists of two distinct knots (Fig. 4), the eastern one of those is again composed of two knots which remind of a primary – secondary hotspot scenario, similar to the situation in 3C 105S. Lonsdale & Barthel (1998) have discussed possible scenarios for such double hotspots which can be created either via a beam jitter model (as proposed for 3C 105S) or a beam deflection model in which the end point of the jet is not marked by the primary hotspot but the secondary, which is still being fed by the deflected, decelerated beam. On the contrary, 3C 227E shows a

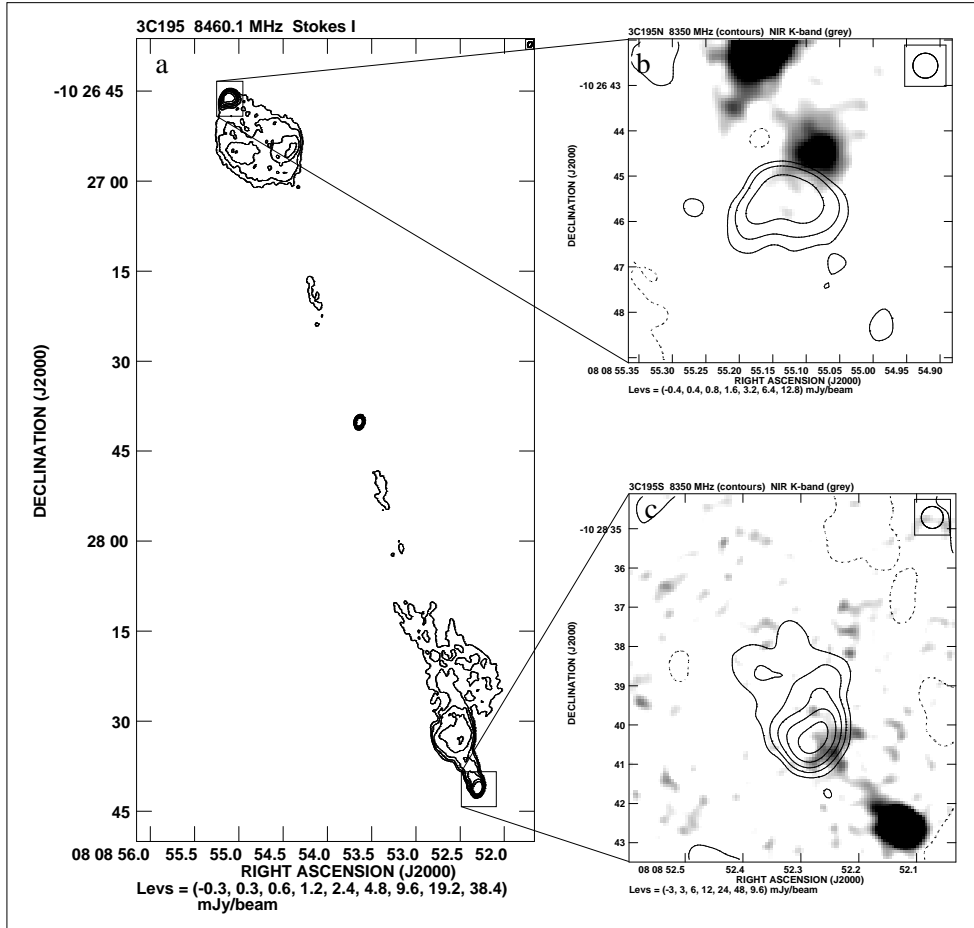


Figure 3. a) 3C 195: entire source, 8.5 GHz, VLA B-array; b) 3C 195N: superposition of VLA A-array data (contours) and ISAAC K-band image (grey), both smoothed to a common resolution of $0''.55 \times 0''.55$; c) 3C 195S: superposition of VLA A-array data (contours) and ISAAC K-band image (grey), both smoothed to a common resolution of $0''.55 \times 0''.55$.

more filamentary structure (Fig. 5), with an extended area of maximum emission. Both hotspots were targets of our optical observations.

2.1.4 3C 327

3C 327 is a Narrow-Line Radio Galaxy (Simpson et al. 1996) at redshift $z = 0.1039$ (Fig. 6a). The eastern hotspot complex consists of a primary knot and a more diffuse secondary one north of it. Both features are embedded in a region of diffuse extended emission (Fig. 6b). The dominant feature in the western hotspot is the slightly curved structure at the very end of the hotspot complex. Leahy et al. (1997) mention the possibility that the brighter structure in the south is part of the radio jet (Fig. 6c). We performed optical observations of both hotspots.

2.1.5 3C 403

The Narrow Line Radio Galaxy 3C 403 at redshift 0.059 belongs to the peculiar class of X-shaped sources which combine two pairs of lobes extending in different directions from the same core. One of these lobe systems is typically more extended and diffuse, while the other one is shorter, brighter and clearly confined. The more extended lobes would be the remainders of an earlier phase of jet

activity, while the shorter, brighter systems would mark the current working direction of the jet. Black et al. (1992) show the overall morphology (their Fig. 13). Hardcastle et al. (1998) suggest that the knot F6 is the primary hotspot in the western lobe. For our detection experiment we focused on the outermost western hotspot (Fig. 7) at the edge of the younger lobe system which is described as an unusually uniform hotspot without apparent substructure by Black et al. (1992).

2.1.6 3C 445

The host galaxy of 3C 445 is a Broad-Line Radio Galaxy (Erculeous & Halpern 1994) at a redshift of 0.05623. This source has been defined as an example of recurrent activity sources. In addition to the bright hotspots in a distance of 315 kpc (north) and 275 kpc (south) of the core, two additional internal hotspots at 47 kpc (north) and 77 kpc (south), well aligned with the outer hotspots and the nucleus are found. These are the characteristics of a Double-Double Radio Galaxy (Lara et al. 1999, Schoenmakers et al. 2000). Both outer hotspots were targets of our study (Figs. 8 & 9).

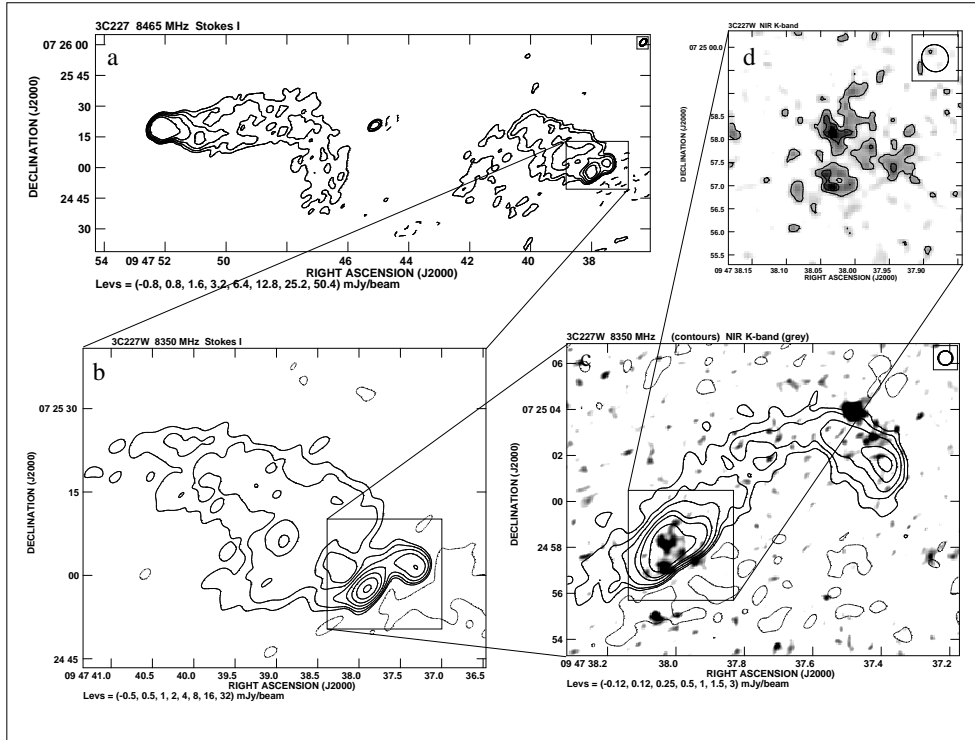


Figure 4. a) 3C 227: entire source, 8.5 GHz, VLA BC-array; b) 3C 227W: 8.4 GHz, VLA B-array; c) 3C 227W: superposition of VLA A-array data (contours) and ISAAC K-band image (grey), both smoothed to a common resolution of $0''.62 \times 0''.62$; d) 3C 227W: NIR K-band emission in original resolution ($0''.58$).

3 OBSERVATIONS AND DATA REDUCTION

3.1 Near Infrared observations with ISAAC

The sample of hotspots listed in Table 1 were observed in the near-IR with ISAAC at the VLT in the J-, H- and K-bands. An exception were the hotspots 3C 227E and W and 3C 327W, which were observed in K-band only as these are the faintest targets in the sample.

The pixel scale of ISAAC in those bands is $0''.148/\text{pix}$. All observations were done in service mode to guarantee optimal weather conditions. In each band the achieved spatial resolution was exceptional, with a FWHM $< 0''.6$ on average. Observations were collected following a random dithering pattern about the science target position. Co-addition of the individual frames was done by applying the standard shift-and-add technique. The total integration time accumulated on the target was on average about 45 minutes per band. In Table 1 a compilation of the ISAAC observations is presented. New data which were not used in the first two papers are marked with an asterisk in Col. 5.

3.2 Optical observations with FORS

Follow-up observations of the hotspot sample were carried out with FORS at the VLT in the R and B bands, with the exceptions of 3C 327W and E, 3C 403W, and 3C 445N. 3C 327E is confused by a background galaxy, 3C 327W is too faint for optical observations and was not detected in the NIR; 3C 403W was not detected in the NIR either and the follow-up optical observations were done in I-band only. Only 3C 445S was in addition observed in the I and U bands. The pixel scale provided by the FORS configuration used with these bands is $0''.20/\text{pix}$. The observation technique used was the same as that described above with ISAAC. The total integration time is about 1 h in the I- and B-bands, 0.5 h in the R-band, and

Table 1. ISAAC observations of the candidate hotspots. Records with an asterisk at the observing date mark new data, which were not used in the first two papers.

source	band	FWHM ($''$)	Magn.	observing date
3C 105S	K	0.43	17.8 ± 0.2	Aug 20 2001
3C 105S	H	0.46	18.3 ± 0.1	Sep 24 2002
3C 105S	J	0.70	20.2 ± 0.2	Aug 23 2002
3C 195N	K	0.40	> 20.5	Apr 09 2001
3C 195N	H	0.34	> 21.6	Jan 21 2003*
3C 195N	J	0.44	> 22.9	Jan 21 2003*
3C 195S	K	0.40	21.3 ± 0.2	Apr 09 2001
3C 195S	H	0.34	> 21.6	Jan 21 2003*
3C 195S	J	0.44	> 22.9	Jan 21 2003*
3C 227E	K	0.47	20.6 ± 0.3	Apr 18 2002
3C 227WE	K	0.58	19.8 ± 0.3	Apr 18 2002
3C 327E	K	0.37	—	May 11 2001
3C 327W	K	0.41	> 22.1	Apr 18 2001
3C 403W	K	0.53	> 22.8	May 11 2003*
3C 403W	H	0.56	> 22.3	Jun 06 2001
3C 403W	J	0.62	> 23.6	Jun 08 2001
3C 445N	K	0.31	19.9 ± 0.3	Jun 06 2001
3C 445N	H	0.38	> 21.4	Sep 18 2001
3C 445N	J	0.46	22.1 ± 0.3	Sep 18 2001
3C 445S	K	0.75	19.0 ± 0.1	Jun 07 2001
3C 445S	H	0.59	19.6 ± 0.2	Jul 06 2001
3C 445S	J	0.49	20.2 ± 0.1	Jun 23 2001

1.6 h in the U-band. The spatial resolution achieved in these observations was on average FWHM $< 0''.6$. In Table 2 a compilation of the FORS observations is presented. New data which were not used in the first two papers are marked with an asterisk in Col. 5.

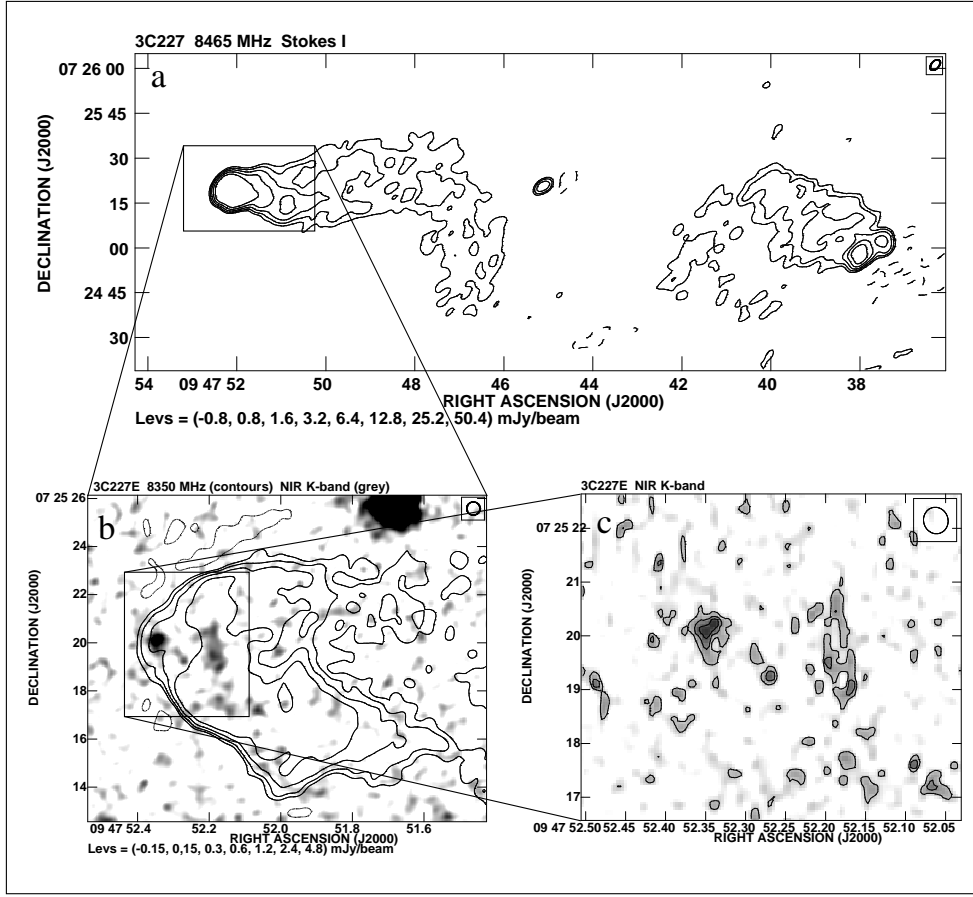


Figure 5. a) 3C 227: entire source, 8.5 GHz, VLA BC-array; b) 3C 227E: superposition of VLA A-array data (contours) and ISAAC K-band image (grey), both smoothed to a common resolution of $0''.55 \times 0''.55$; c) 3C 227E: NIR K-band emission in original resolution ($0''.47$).

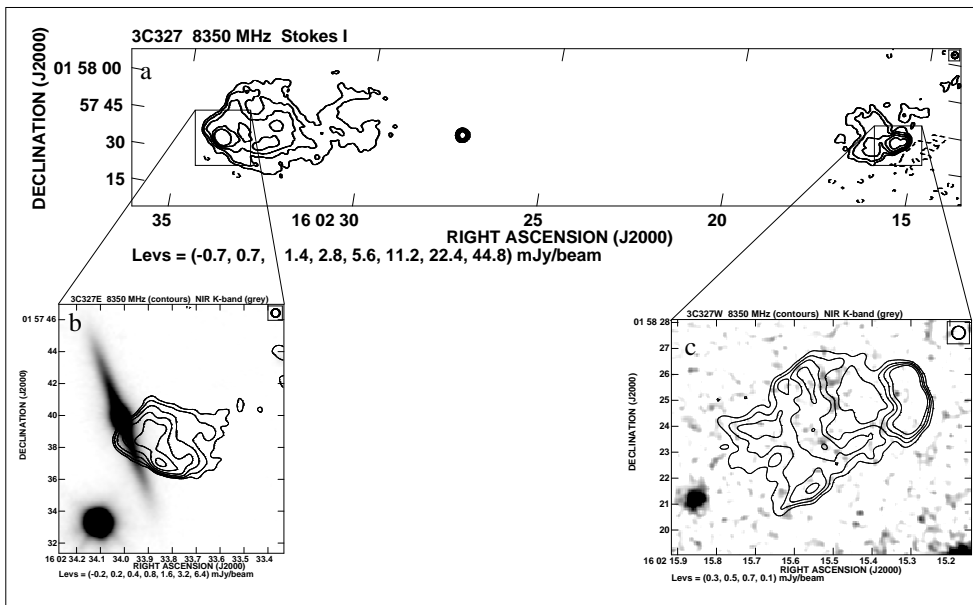


Figure 6. a) 3C 327: entire source, 8.4 GHz, VLA BC-array; b) 3C 327E: superposition of VLA A-array data (contours) and ISAAC K-band image (grey), both smoothed to a common resolution of $0''.52 \times 0''.52$; c) 3C 327W: superposition of VLA A-array data (contours) and ISAAC K-band image (grey), both smoothed to a common resolution of $0''.50 \times 0''.50$.

Table 2. FORS observations of the candidate hotspots. Records with an asterisk at the observing date mark new data, which were not used in the first two papers.

source	band	FWHM ($''$)	Magn.	observing date
3C 105S	R	0.6	22.8 0.1	Nov 26 2003*
3C 105S	B	0.74	24.5 0.3	Nov 26 2003*
3C 195N	R	0.68	> 25.8	Dec 18 2003*
3C 195N	B	0.68	> 25.7	Nov 30 2003*
3C 195S	R	0.68	25.4 0.2	Dec 18 2003*
3C 195S	B	0.68	> 25.7	Nov 30 2003*
3C 227WE	R	0.8	24.4 0.2	Dec 18 2003*
3C 227WE	B	0.8	25.4 0.2	Dec 18 2003*
3C 227E	R	0.8	23.9 0.2	Dec 18 2003*
3C 227E	B	0.8	25.6 0.2	Dec 18 2003*
3C 403W	I	0.65	> 24.0	Sep 14 2001
3C 445S	I	0.66	21.5 0.1	Sep 15 2001
3C 445S	R	0.58	22.0 0.2	Nov 02 2002
3C 445S	B	0.56	22.9 0.2	Nov 02 2002
3C 445S	U	0.72	23.2 0.2	Jul 03 2003*

3.3 Radio data

Between April 2002 and January 2004, we observed all targets, with the exception of 3C 227 and 3C 327, with the VLA at 1.4, 5.0 and/or 8.4 GHz either in A or B configuration, in order to construct multi-frequency radio continuum spectra of the hotspots. For the source 3C 195 we analysed further archival data at 5.0 and 15.0 GHz. Information on the observing runs are provided in Table 3. The data reduction was carried out following the standard procedures for the VLA implemented in the NRAO AIPS package.

For each observing run about 3-5 min, depending on the frequency, were spent on the primary calibrator 3C 286. Secondary calibrators, chosen to minimize the telescope slewing time were observed for 1.5 min every 5 min. The flux densities were calibrated according to the scale of Baars et al. (1978). At 1.4 GHz it was necessary to image a few confusing sources falling into the primary beam in order to have an accurate measurement of the flux density. The final images were produced after a few phase-only self-calibration iterations.

In addition, these data were complemented by archive data from the NRAO VLA archive, observed as part of the project AB534, which were originally published by Black et al. (1992) and Leahy et al. (1997). In Table 3 a compilation of the VLA observations is presented. New data which were not used in the first two papers are marked with an asterisk in Col. 5.

4 RESULTS

To identify a possible NIR/optical counterpart of the radio hotspots we superimposed the radio images with the NIR/optical data. To this purpose, the optical images were brought on the same grid and orientation as the radio images. Several sources of the USNO-B1.0 survey (Monet et al. 2003) were identified in the images and used as reference sources for a transformation of the coordinate systems using AIPS task XTRAN. The alignment between radio and optical images was cross-checked by superposition of point-like radio and optically emitting regions like the host galaxies (when covered by the optical image) or other AGN in the field. We estimate the typical remaining uncertainties to be of the order of 0.4. In order to assure the correct determination of flux densities at the various wavebands

Table 3. VLA observations of the candidate hotspots

source	frequency [GHz]	conf.	beamsize [$''$ $''$]	beam p.a. [°]	obs. date
3C 105S	1.4	A	1.23 1.18	35	Jul 19 2003*
3C 105S	4.8	A	0.37 0.35	78	Jul 19 2003*
3C 105S	8.4	A	0.54 0.26	71	May 25 1990
3C 195N, S	1.4	B	6.22 4.01	20	Jan 17 2004*
3C 195N, S	4.9	B	1.98 1.19	31	Aug 18 1986
3C 195N, S	8.4	B	1.04 0.67	15	Jan 17 2004*
3C 195N, S	8.4	A	0.32 0.21	12	Aug 03 1991
3C 195N, S	15.0	B	0.50 0.35	3	Sep 02 2006*
3C 227W, E	8.4	A	0.38 0.22	50	May 25 1990
3C 327W	8.4	A	0.35 0.22	48	May 25 1990
3C 403W	1.4	A	1.82 1.37	58	Apr 18 2002
3C 403W	4.8	A	0.47 0.35	55	Apr 18 2002
3C 403W	8.4	B	0.97 0.85	45	Apr 07 1989
3C 445N	1.4	A	1.43 1.04	15	Jul 19 2003*
3C 445N	4.8	A	0.46 0.37	23	Jul 19 2003*
3C 445N	8.4	A	0.27 0.24	31	Apr 18 2002
3C 445S	1.4	A	1.42 1.02	11	Jul 19 2003*
3C 445S	4.8	A	0.46 0.37	23	Jul 19 2003*
3C 445S	8.4	A	0.26 0.22	12	Apr 18 2002*

Table 4. VLA flux densities and angular sizes of the candidate hotspots

source	S _{1.4} [mJy]	S _{4.8} [mJy]	S _{8.4} [mJy]	S ₁₅ [mJy]	θ_{maj} [$''$]	θ_{min} [$''$]	P _{8.4GHz} [10 ²³ W/Hz]
3C 105S	2790	1268	873		7.0	5.0	169
3C 195N	250	90	45	22	1.7	1.4	13.7
3C 195S	440	140	67	34	1.8	1.1	20.3
3C 227E			47		1.7	1.4	8.5
3C 227WE			37		1.9	1.2	3.8
3C 327W			21		2.4	1.0	5.6
3C 403W	94	50	33		5.4	4.1	4.7
3C 445N	160	58	35		3.5	2.0	2.6
3C 445S	520	135	81		6.0	3.0	6.0

in the same regions, all images were convolved to a common resolution using AIPS task CONVL. The hotspot flux densities and angular sizes were measured in the images using the AIPS task JMFIT which performs a Gaussian fit, while in extended structures the flux density was obtained by TVSTAT. Observational parameters of the hotspots are reported in Tables 1 and 2 for NIR/optical observations and Table 4 for the radio observations. The main uncertainties of the flux density measurements come from amplitude calibration errors, usually between 3% and 5%, while the r.m.s. noise level in the image plane is not relevant.

The optical magnitudes were determined using the IDL-based task ATV in various iterations to identify the optimum integration area around the targets and correcting for any remaining local background instabilities, which however dominate the measurement errors. Magnitudes were subsequently transformed into jansky using standard formulae (Campins, Rieke & Lebofsky 1985; Allen 1972).

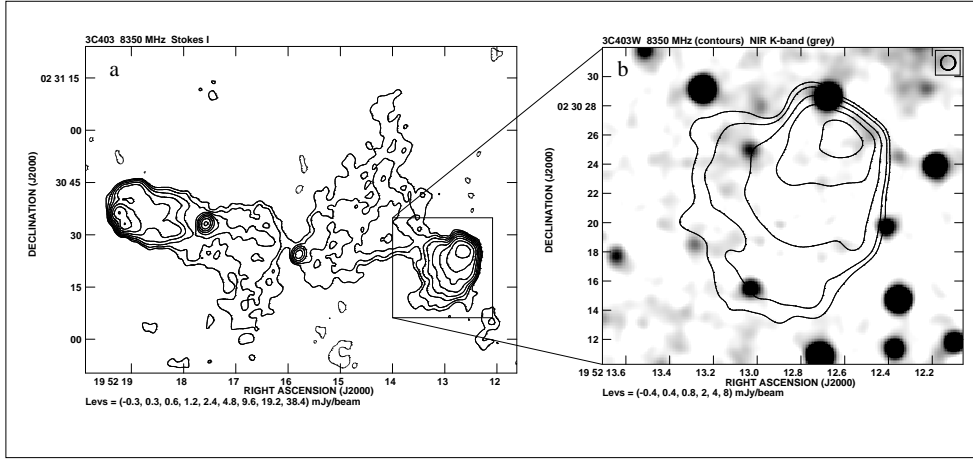


Figure 7. 3C 403: entire source, 8.4 GHz, VLA B-array; b) 3C 403W: superposition of VLA B-array data (contours) and ISAAC K-band image (grey), smoothed to a common resolution of $190'' \times 190''$.

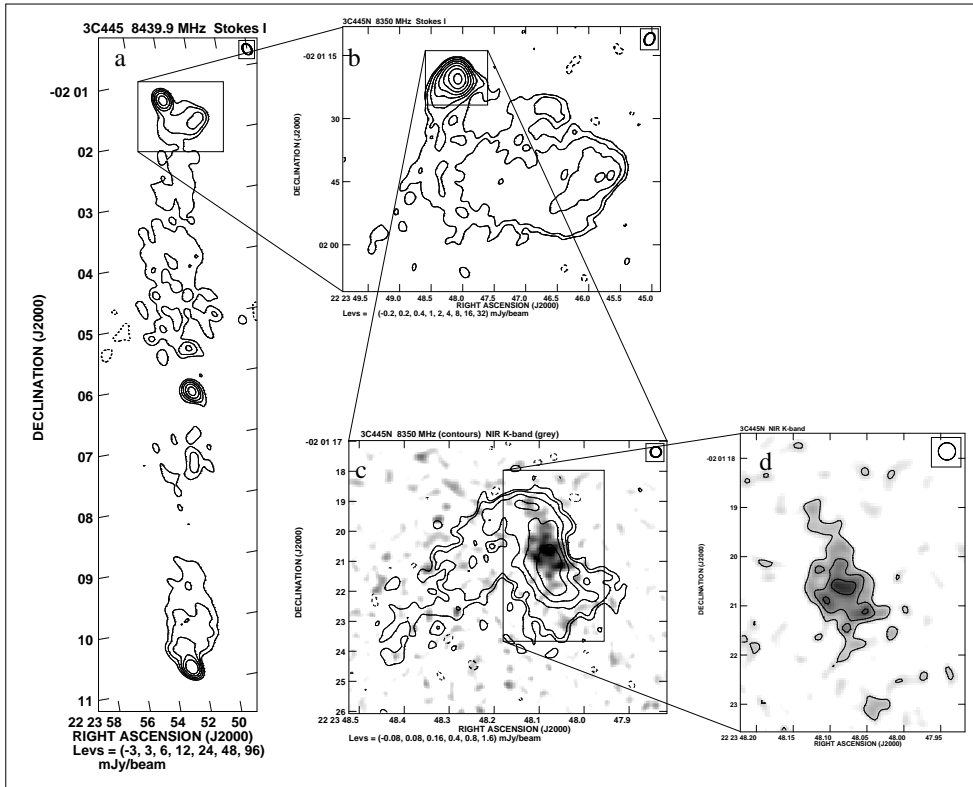


Figure 8. 3C 445: entire source, 8.4 GHz, VLA C-array; b) 3C 445N: 8.4 GHz, VLA B-array; c) superposition of VLA A-array data (contours) and ISAAC K-band image (grey), both smoothed to a common resolution of $0.35'' \times 0.35''$; d) 3C 445N: NIR K-band emission in original resolution ($0.31''$).

4.1 Optical detections

We unambiguously detected optical emission connected with the radio emission in four of the nine hotspots of the final sample (3C 327E excluded): 3C 105S, 3C 227W, 3C 445N and 3C 445S. In addition there are two doubtful cases (3C 195S and 3C 227E), for which the successful detection of an NIR counterpart cannot be confirmed yet on the basis of the present imaging data. No detections were found for 3C 195N, 3C 327W and 3C 403W. The finally reached detection rate is 67% (decreasing to 45% if the optical counterparts of 3C 195S and 3C 227W are not confirmed). Such a

success rate is much higher than usually found in the literature and may be due to the low magnetic field strengths in these, specifically selected, hotspots.

In Figs. 1 and 3 - 9 we present the NIR K-band emission for each of our target superimposed to the radio image, both smoothed to the same resolution. In case of a large discrepancy between the resolutions of the convolved and the original images the optical emission is also shown at its original resolution.

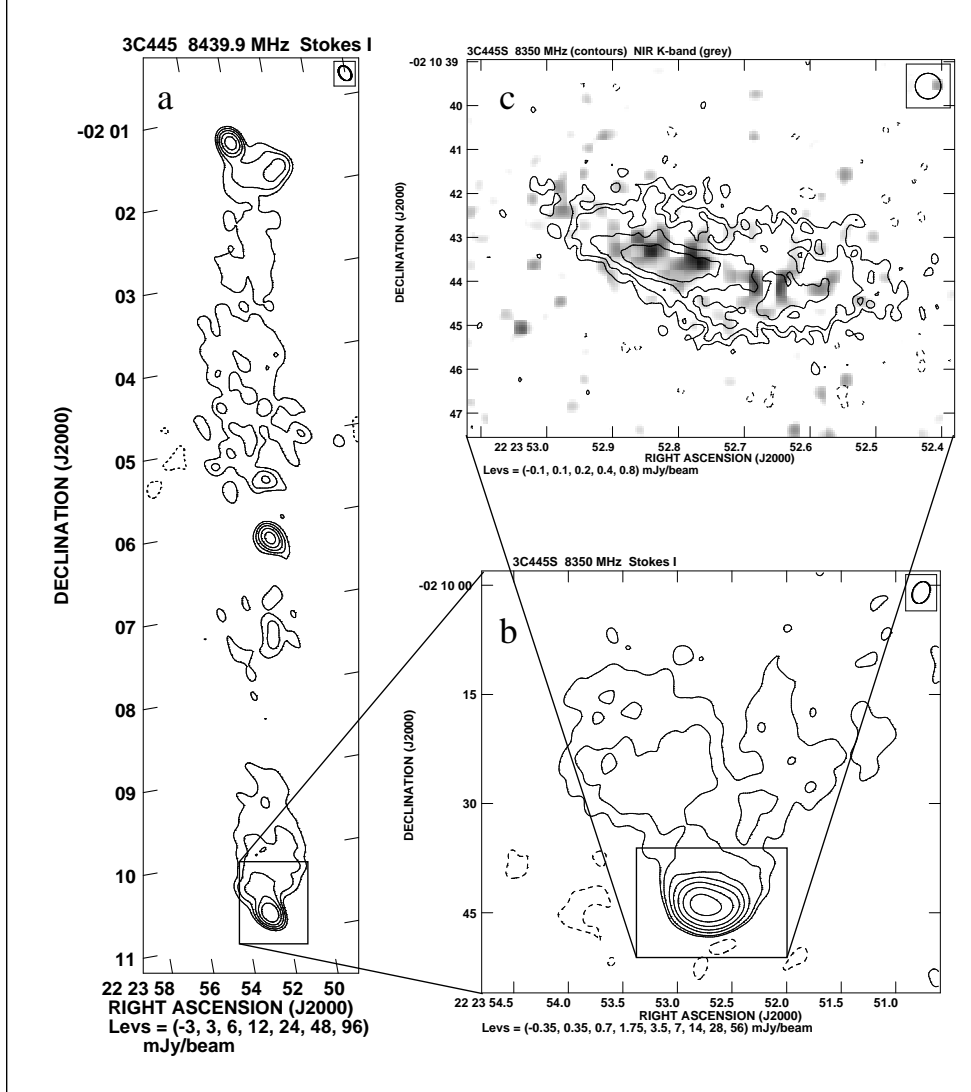


Figure 9. 3C 445: entire source, 8.4 GHz, VLA C-array; b) 3C 445S: 8.4 GHz, VLA B-array; c) superposition of VLA A-array data (contours) and ISAAC K-band image (grey), both smoothed to a common resolution of $0''.58 \times 0''.58$.

4.2 Comments on individual sources

4.2.1 3C 105

The southern hotspot of 3C 105 is characterized by three well-resolved asymmetric sub-structures, each one with a clear NIR counterpart (Fig. 2). The NIR emission at $\alpha = 04^h07^m25^s.22$, $\delta = 03^\circ40'51''.2$ does not have a radio counterpart and is considered to be an unrelated background source. The northern and southern components are located $3''.8$ (6.2 kpc) and $2''.1$ (3.4 kpc) respectively from the central component, which is also the brightest one in radio, while in the optical band the southern component accounts for the higher flux density. All components have a spectral index between 8.4 GHz and K-band of $\alpha = 1.0$. A more detailed analysis of this impressive hotspot complex will be presented in a forthcoming paper.

4.2.2 3C 195

The high-resolution image of the northern hotspot of 3C 195 reveals the detected NIR emission to be unrelated to the radio emission. The situation in the southern hotspot is more difficult to judge. The NIR observations show extended emission within the contours of the radio emission. However, the shape of the optical emission seems to be unrelated to the radio morphology and its barycentre is shifted by about one beam size to the southwest with respect to the radio peak. This and the relative weakness of the NIR emission make a successful detection arguable.

4.2.3 3C 227

The western lobe is characterized by two asymmetric radio hotspots located about $10''$ (16 kpc) apart from each other. Their flux density ratio is $S_{WE}/S_{WW} = 3.3$. Only the eastern component has a clear positional counterpart with the NIR emission, while the situation of the westernmost component is more uncertain with the optical counterpart located outside the compact region of the ra-

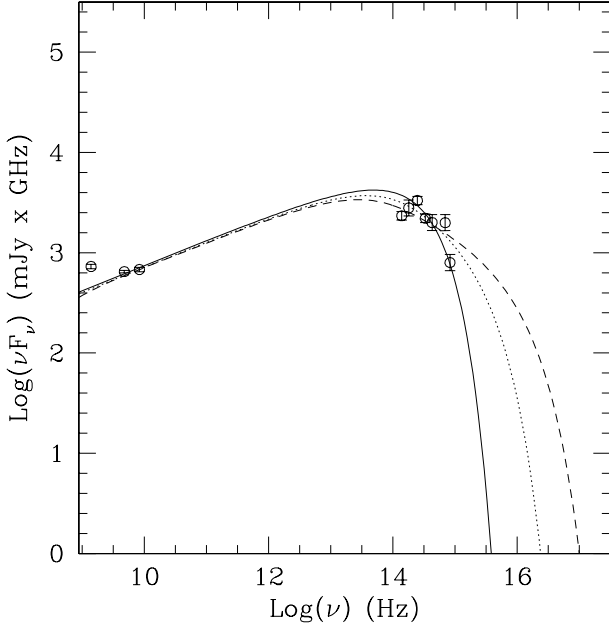


Figure 10. Examples of model spectral energy distributions of the hotspot of 3C 445S for three different break frequencies (assuming $\alpha_{inj} = 0.75$) to illustrate a comparison between model expectations and data. The models are normalised at the radio flux densities. The different break frequencies are $\nu_b = 5.0 \cdot 10^4$ Hz, $\nu_c = \nu_b = 1$ (solid line); $\nu_b = 1.2 \cdot 10^4$ Hz, $\nu_c = \nu_b = 50$ (dotted line) and $\nu_b = 7.0 \cdot 10^3$ Hz, $\nu_c = \nu_b = 400$ (dashed line).

radio hotspot (Fig. 4c). The spectral indices between 8.4 GHz and K-band are $\alpha_{WE} = 0.9$ and $\alpha_{WW} > 1.0$ for the eastern and the western components (assuming that the optical emission is not connected with the western radio component), respectively. Hardcastle, Croston & Kraft (2007) found X-ray emission from both the eastern and western components of the western hotspot of 3C 227. Remarkably the radio and X-ray peaks are not coincident and these authors discuss possible consequences of the positional offsets on the mechanisms responsible for the observed emission. Clearly deeper optical observations would greatly help to constrain positional offsets between the counterparts of the hotspot at different wavelengths and to eventually confirm the detection of the optical counterpart of the western component of 3C 227W.

Also the eastern lobe shows underlying NIR emission in the area of its hot spot (Fig. 5). These two distinct features are both relatively weak. The eastern component (Fig. 5c) at the tip of the lobe is basically point-like, the elongated feature to the west is fainter and roughly coincides with the region of maximum radio brightness. In principle, this extended NIR emission could derive from the radio hotspot, although in order to verify the optical detection of the hotspot beyond any doubt much deeper optical imaging is required. A comparison with the X-ray emission reported by Hardcastle et al. (2007) remarkably shows coincident positions of the extended NIR emission with a chain of point-like X-ray emitters (Fig. 4 in Hardcastle et al.).

4.2.4 3C 327

The western hotspot does not show any significant NIR counterpart. This results in a lower limit for the spectral index $\alpha > 1.0$. The image of the eastern hotspot is confused by an underlying spiral

galaxy. As it is therefore impossible to decide whether the hotspot emission reaches up to the NIR band, 3C327E has been removed from our sample.

4.2.5 3C 403

This source at relatively low Galactic latitude is situated in a star-rich environment. None of the significant NIR detections within the radio contours seems to be related to the radio hotspot. Kraft et al. (2005) report extended X-ray emission from the western lobe of 3C 403 and suggest inverse Compton scattering of beamed IR/optical photons from the active nucleus. On the other hand, these authors find several X-ray and optical emitting knots associated with the eastern jet, which however are not covered by our data.

4.2.6 3C 445

Both hotspots of 3C 445 are characterized by extended emission, about $2.5 \cdot 1.5$ (2.7 kpc 1.6 kpc) for the North and about $7.0 \cdot 4.0$ (7.5 kpc 4.3 kpc) for the South, detected also in the optical band. The northern one is elongated in the NE-SW direction (Fig. 8c), while the southern hotspot shows an arc-like structure (Fig. 9c). Both hotspots have a spectral index between 8.4 GHz and K-band of $\alpha = 0.9$. Prieto et al. (2002) underlined the importance of 3C 445S that is a clear example of a hotspot whose properties are difficult to reproduce with a simple shock-acceleration model. The optical images of the hotspot region show an arc-like structure with bright compact knots, identified as *local particle accelerators*, embedded into more diffuse optical emission. These knots are interpreted as the result of a small-scale dentist drill which deposits the kinetic energy of the jet in several locations, while the diffuse emission may indicate that in-situ particle re-acceleration, due to Fermi-II mechanisms, is at work in the whole hotspot region.

A detailed analysis of these hotspots will be presented in a forthcoming paper.

5 SYNCHROTRON SPECTRA

In low-power radio hotspots the radiative life-times of the electron populations is expected to be longer than in high-power radio hotspots, likely due to lower values of the magnetic field (Blundell et al. 1999; Brunetti et al. 2003). In such a situation, the break frequency may occur at IR and optical wavelengths.

In the context of the shock-acceleration scenario two important frequencies exist in the synchrotron spectrum of hotspots: the break frequency, ν_b , that marks the maximum frequency of the synchrotron emission from the oldest electrons still confined in the hotspot volume, and the cut-off frequency, ν_c , that marks the maximum frequency of the synchrotron radiation emitted by the electrons accelerated at the shock (e.g. Meisenheimer et al. 1989; Brunetti et al. 2002). Constraining these frequencies provides fundamental implications on the efficiency of the acceleration of particles at the shock and on the physical conditions in the shock region (e.g. magnetic field strength). Reliable constraints can be obtained if the optical data points sample the spectrum at $\nu > \nu_b$ (e.g., Meisenheimer et al. 1997; Brunetti et al. 2001; Wilson, Young & Shopbell 2001), i.e. in the case of hotspots emitting most of their synchrotron radiation at mm–far-IR wavelengths. On the other hand, the bulk of the synchrotron radiation from the hotspots in our sample is emitted at optical wavelengths and thus it is possible to

constrain only v_b ; an example is given in Fig. 10, where we show the case of 3C 445S.

Thus, as $v_b = v_c$ is poorly constrained we decided to fit the spectra of the hotspots with a simple single-injection synchrotron model (Jaffe & Perola 1973) that is an over-simplification (with $v_b = v_c$) but still provides a viable approach to obtain statistical measures of v_b or upper limits to v_b in the case of optical non-detections. More specifically, for 3C 445N and 3C 445S we did not consider the flux density at 1.4 GHz because of the strong contamination from the lobe. The resulting break frequencies for most of the hotspots range between 10^5 and 10^6 GHz. The upper limit of the break frequency obtained for hotspots without optical counterparts is $6.5 \cdot 10^4$ GHz. In the case of 3C 327W the availability of only two data points did not allow us to perform any synchrotron model on their spectrum. Model fits to the spectra of the hotspots are shown in Fig. 11, while fit parameters are reported in Table 5.

From the break frequency ν_{br} [GHz] it is possible to determine the radiative age t_{rad} [Myr] of the electron populations, once the magnetic field strength B [μ G] is known, by:

$$t_{rad} \approx 1610 B^{-3/2} \frac{1}{\nu_{br} (1+z)} \quad (1)$$

where the magnetic field equivalent to the cosmic microwave background has been neglected being much smaller than the typical magnetic fields in hotspots. These fields were computed assuming equipartition conditions (Table 5), following the approach of Brunetti, Setti & Comastri (1997) assuming a minimum Lorentz factor of the relativistic electrons $\gamma_{min} = 100$, equal proton and electron energy densities, and an ellipsoidal geometry with a filling factor of unity (i.e. the hotspot volume is fully and homogeneously filled by relativistic plasma).

If we consider the break frequency inferred from the fits we find that the radiative ages of the electron populations with detected optical emission located in such magnetic fields are of the order of 10^3 years (Table 5). These relatively short time scales imply either that the injection of relativistic plasma from the jet is not continuous but happens on a period of $\sim 10^3$ years, or that adiabatic expansion in the hotspot takes place in $\sim 6 \cdot 10^3$ years and the emission from older electrons is thus just faded away.

In the second scenario, however, adiabatic expansion is expected to affect the properties of the emitting plasma in a time scale that should be significantly larger than a crossing time-scale of the hotspot at the speed of sound (or Alfvén speed), $l_{HS} = c_s > l_{HS} = c$. The crossing time scale should be smaller than (or comparable to) the ages measured in our hotspots yielding the following condition:

$$\frac{B}{B_{eq}}^{-3/2} \frac{l_{HS}}{\text{kpc}} < 1 \quad (2)$$

that would require either that the magnetic fields in the hotspots are substantially smaller than the equipartition field, or that compact (sub-kpc), over-pressured, emitting regions, are embedded in the hotspot. If these two conditions are not realised the adiabatic losses are not fast enough to act within a time-scale of $\sim 10^3$ years and the absence of older electrons in the hotspots is not easy to account for in the context of a scenario of continuous jet activity. On the other hand, the radiative age of the hotspots measured from the synchrotron break frequency is based on the assumption that electrons, accelerated at the shock, cool in the post shock region in absence of any additional (efficient) re-acceleration mechanism. This might not be the case since the evidence for diffuse synchrotron emission on kpc scale in several hotspots in our sample suggests that in situ (additional) particle re-acceleration mechanisms may be at work in

Table 5. Physical parameters

Source	ν_{br} [GHz]	α	B_{eq} [μ G]	t_{rad} [10^3 yr]	distance [kpc]	
3C 105S	1.37	1.0	0.75	75	6.4	278
3C 195N	< 2.7	1.0	0.95	62	> 6.0	117
3C 195S	5.34	1.0	1.00	78	3.0	127
3C 227WE	3.0	1.0	0.65	126	2.0	173
3C 227E	1.14	1.0	0.75	99	1.5	169
3C 403W	< 2.95	1.0	0.55	38	> 39	52
3C 445N	6.63	1.0	0.85	60	4.1	315
3C 445S	8.40	1.0	0.80	68	2.8	275

the hotspot volume. In this case the radiative ages estimated from the break frequency should represent a lower limit to the real age of the electrons. For instance, Prieto et al. (2002) suggested that Fermi II mechanisms with a typical electron re-acceleration time-scale $\sim 10^4$ years are required to explain the diffuse optical emission in the hotspot 3C 445S. If these mechanisms are slightly more efficient than previously thought they may contribute to balance the radiative losses of the emitting particles, in which case electrons injected in the hotspot volume more than 10^3 years ago may still be emitting at optical frequencies.

6 SUMMARY

We present new data of a sample of low-power hotspots ($P_{1.4\text{GHz}} \sim 10^{25}$ W/Hz) observed at several NIR and optical bands, complemented by high-resolution radio observations. From this investigation we found:

Of the 9 targeted hotspots at least 4 show a clear detection at the NIR K-band, in several cases up to the optical (R, B) bands. An additional two hotspots show NIR features which cannot yet safely be identified as the optical counterpart of the radio hotspot and will need deeper observations. In any case this results in unprecedented detection rates between 45% and 67%.

This high detection rate is attributed to the high break frequencies (10^5 to 10^6 GHz) of the continuum spectra of the detected sources that emit the bulk of their synchrotron emission at optical wavelength. High values of the break frequencies are indeed expected in the class of low-power hotspots (Blundell et al. 1999; Brunetti et al. 2003). For comparison, typical parameters of previously known optical hotspots reported in the literature have equipartition fields $> 100 \mu\text{G}$ and break frequencies in the range of 10^3 to 10^4 GHz.

The large values of the synchrotron break frequencies in optically detected hotspots in our sample imply that the emitting electrons have been injected in the hotspot volume less than 10^3 years ago. A first obvious possibility to explain the lack of older electrons in the emitting volume is an intermittent activity of the jet with a time-scale $\sim 10^3$ years. A second possibility is that the emission from older electrons in the hotspot volume is fading away due to fast adiabatic losses, in which case the optical emission is expected to be produced from compact (sub-kpc) and over-pressured knots. Alternatively, in-situ Fermi-II mechanisms, with a particle re-acceleration time scale $\sim 2.5 \cdot 10^3$ years, partially balance the radiative losses of electrons. In this case, the radiative age from the

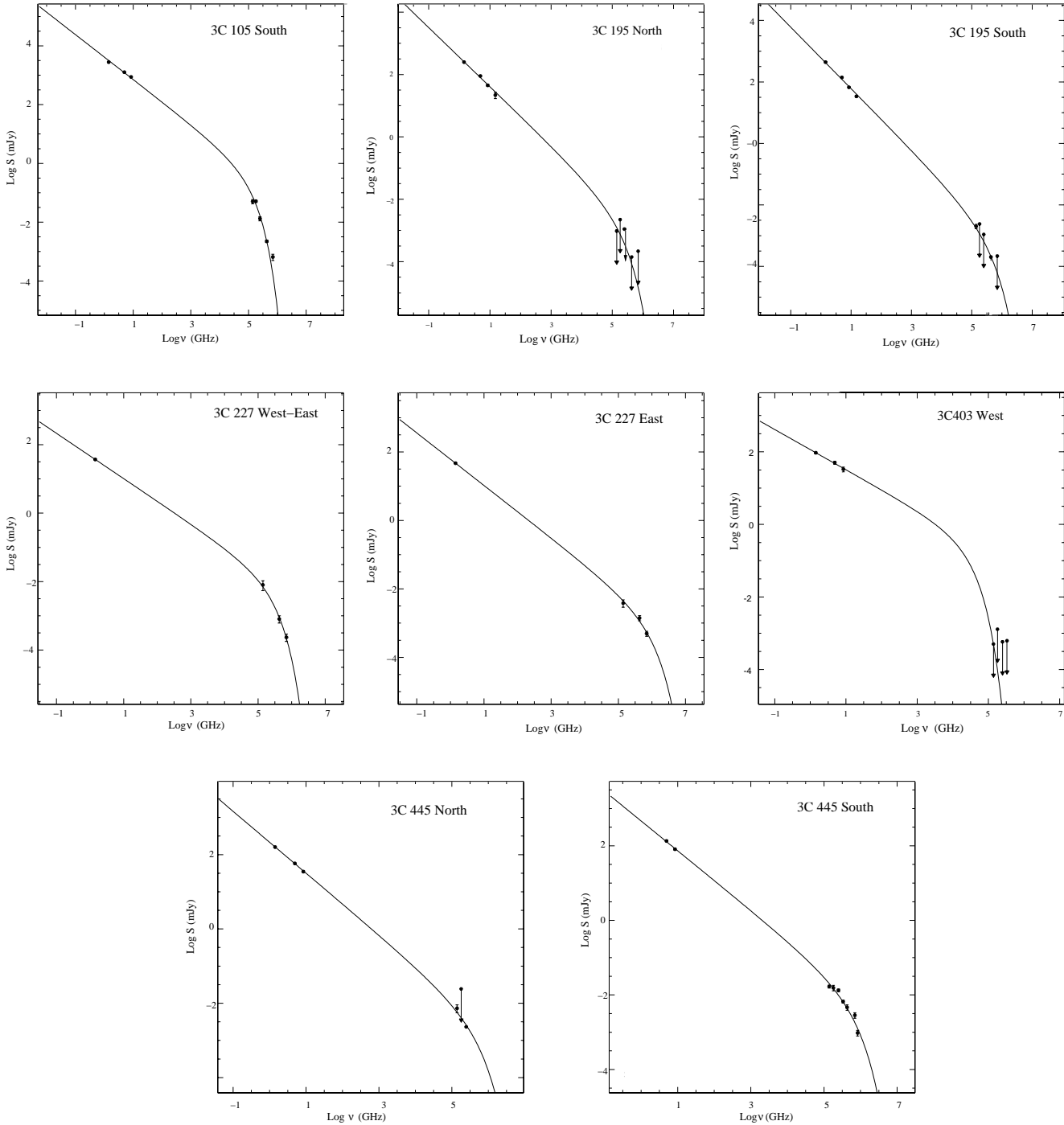


Figure 11. Synchrotron fits to the spectra of the 8 hotspots with sufficient measurements. 3C 327W was excluded as only one radio frequency and one upper limit at NIR K-band is known.

measurement of the synchrotron break frequency should be considered a lower limit to the real age of the particles.

In almost all cases the detected NIR/optical emission is extended between 3 and 8 kpc. It breaks down in multiple substructure indicating that we may be over-resolving the emission. The diffuse emission suggests that in situ re-acceleration mechanisms may be at work in the hotspot volume, as previously pointed out in 3C 445S (Meisenheimer et al. 1997, Prieto et al. 2002). This would further

suggest that the radiative ages measured from the synchrotron break differ from the real ages of the emitting particles.

ACKNOWLEDGEMENTS

The National Radio Astronomy Observatory is a facility of the National Science Foundation operated under cooperative agreement

by Associated Universities, Inc. This work has made use of the NASA/IPAC Extragalactic Database NED which is operated by the JPL, Californian Institute of Technology, under contract with the National Aeronautics and Space Administration.

Tadhunter C.N., Morganti R., di Serego Alighieri S., Fosbury R.A.E.,
Danziger I.J., 1993, MNRAS, 263, 999
Thomson R.C., Crane P., Mackay C.D., 1995, ApJ, 446, L93
Wall J.V., Peacock J.A., 1985, MNRAS, 216, 173
Wilson A.S., Young A.J., Shopbell P.L., 2001, ApJ, 547, 740

REFERENCES

- Allen C.W., 1981, 'Astrophysical Quantities', 3rd reprinted edition, The Athlone Press, University of London, Great Britain
Baars J.W.M., Genzel R., Pauliny-Toth I.I.K., Witzel A., 1977, A&A, 61, 99
Bell A.R., 1978, MNRAS, 182, 147
Black A.R.S., Baum S.A., Leahy J.P., Perley R.A., Riley J.M., Scheuer P.A.G., 1992, MNRAS, 256, 186
Blundell K.M., Rawlings S., Willott C.J., 1999, AJ, 117, 677
Brunetti G., Bondi M., Comastri A., Pedani M., Varano S., Setti G., Hardcastle M.J., 2001, ApJ, 561, 157
Brunetti G., Bondi M., Comastri A., Setti G., 2002, A&A, 381, 795
Brunetti G., Mack K.-H., Prieto M.A., Varano S., 2003, MNRAS, 345, 40
Brunetti G., Setti G., Comastri A. 1997, A&A, 325, 898
Campins H., Rieke G.H., Lebofsky M.J., 1985, AJ, 90, 896
Cox C.L., Gull S.F., Scheuer P.A.G., 1991, MNRAS 252, 558
Cheung K., Kim C.S., Song J., 2005, ApJ, 628, 104
Eracleous M., Halpern J.P., 1994, ApJS, 90, 1
Georganopoulos M., Kazanas D., 2003, ApJ, 594, 27
Gopal-Krishna, Subramanian P., Wiita P.J., Becker P.A., 2001, A&A, 377, 827
Hardcastle M.J., Alexander P., Pooley G.G., Riley J.M., 1998, MNRAS, 296, 445
Hardcastle M.J., 2001, A&A, 373, 881
Hardcastle M.J., 2003, NewAR, 47, 649
Hardcastle M.J., Harris D.E., Worrall D.M., Birkinshaw M., 2004, ApJ, 612, 729
Hardcastle M.J., Croston J.H., Kraft R.P., 2007, ApJ, 669, 893.
Harris D.E., Carilli C.L., Perley R.A., 1994, Nat, 367, 713
Heavens A.F., Meisenheimer K., 1987, MNRAS, 225, 335
Jaffe W.J., Perola G.C., 1973, A&A, 26, 423
Kapahi V.K., Athreya R.M., van Breugel W., McCarthy P.J., Subrahmanya C.R., 1998, ApJS, 118, 275
Kraft R.P., Hardcastle M.J., Worrall D.M., Murray S.S., 2005, ApJ, 622, 149
Kundt W., 1996, Lecture Notes in Physics, 471, 1
Lähteenmäki A., Valtaoja E., 1999, AJ, 117, 1168
Lara L., Márquez I., Cotton W.D., Feretti L., Giovannini G., Marcaide J.M., Venturi T., 1999, A&A, 348, 699
Leahy J.P., Black A.R.S., Dennett-Thorpe J., Hardcastle M.M., Komissarov S., Perley R.A., Riley J.M., Scheuer P.A.G., 1997, MNRAS, 291, 20
Lonsdale C.J., Barthel P.D., 1998, AJ, 115, 895
Meisenheimer K., Röser H.-J., 1986, Nat, 319, 459
Meisenheimer K., Röser H.-J., Hiltner P.R., Yates M.G., Longair M.S., Chini R., Perley R.A., 1989, A&A, 219, 63
Meisenheimer K., Yates M.G., Röser H.-J., 1997, A&A, 325, 57
Meisenheimer K., 2003, NewAR, 47, 495
Monet D.G. et al., 2003, AJ, 125, 984
Morganti R., Killeen N.E.B., Tadhunter C.N., 1993, MNRAS, 263, 1023
Morganti R., Oosterloo T.A., Reynolds J.E., Tadhunter C.N., Migenes V., 1997, MNRAS, 284, 541
Morganti R., Oosterloo T.A., Tadhunter C.N., Aiudi R., Jones P., Villar-Martin M., 1999, A&AS, 140, 355
Neff S.G., Roberts L., Hutchings J.B., 1995, ApJS, 99, 349
Prieto M.A., Kotilainen J.K., 1997, ApJ, 491, L77
Prieto M.A., Brunetti G., Mack K.-H., 2002, Sci, 298, 193
Scheuer P.A.G., 1995, MNRAS, 277, 331
Schoenmakers A.P., de Bruyn A.G., Röttgering H.J.A., van der Laan H., Kaiser C.R., 2000, MNRAS, 315, 371
Simpson C., Ward M., Clements D.L., Rawlings S., 1996, MNRAS, 281, 509